Hindawi
Advances in Civil Engineering
Volume 2020, Article ID 8824914, 10 pages
https://doi.org/10.1155/2020/8824914

Research Article

Experimental Investigation of Dynamic Compression Mechanical Properties of Frozen Fine Sandstone

Jiehao Wu, Haibo Wang, Qi Zong, and Ying Xu

School of Civil Engineering and Architecture, Anhui University of Science and Technology, Huainan, Anhui 232001, China

Correspondence should be addressed to Jiehao Wu; jhwu1991@163.com

Received 20 June 2020; Revised 10 August 2020; Accepted 25 August 2020; Published 8 September 2020

Academic Editor: Fengqiang Gong

Aiming at the dynamic mechanical properties of weakly cemented fine sandstone in the rich water-bearing strata in western China under dynamic loading, a 50 mm rod diameter separation Hopkinson pressure bar (SHPB) test was used to study the Paleogene fine sandstone in a coal mine in Ningxia. The system carried out the impact compression tests of −15°C, −20°C, and −30°C and the average strain rate of 28 s^{-1}–83 s^{-1} and obtained the dynamic compressive strength of the frozen fine sandstone specimens under different test conditions. The strain curve and the fracture morphology were analyzed for the relationship between dynamic peak stress, peak strain, dynamic strength growth coefficient (DIF), and fracture morphology and strain rate. The results show that the peak stress of frozen fine sandstone increases from the decrease of freezing temperature under the same average strain rate. The peak stress of the specimen increases from the increase in the average strain rate of the same freezing temperature. The failure modes of specimen are mainly divided into axial splitting tensile failure and compression crushing failure. To the splitting tensile failure and the compression crushing failure, the main factors determining the two failure modes are the strain rate, while the temperature affects the severity of the impact damage. In the load strain rate and temperature range, the DIF of the frozen fine sandstone is linearly correlated with the strain rate, and the lower the temperature, the slower the growth rate of the DIF.

1. Introduction

In the construction of coal mine shafts in western China, Paleogene fine sandstone is often encountered, which easily disintegrates in water to form quicksand, seriously endangering the safety of workers and equipment at the working face [1, 2]. The freezing method is widely used in shaft construction in water-rich strata due to its effective water shutoff [3–5]. The frozen bedrock section of the shaft is usually constructed by drilling and blasting. However, the Paleogene fine sandstone is mostly nondiagenetic or slightly semidiagenetic and has poor cementation. The study of the dynamic mechanical properties of frozen fine sandstone under a dynamic load is of great value of practical applications because it ensures the safety of the frozen sidewalls and guides drilling and blasting construction.

Until now, research on the freezing of Paleogene fine sandstones in western China has mainly focused on its static physical and mechanical properties. Using freezing shaft construction in the Hujiahe Coal Mine in the Binchang Mining Area, Shaanxi, China, as the study area, Yang and Lv [6] experimentally studied the uniaxial and triaxial mechanical properties of the sandy mudstone in the main shaft and investigated the variation patterns of the strength and deformation properties under different temperatures and confining pressures. Liu et al. [7] studied the strength properties of red sandstone with a weak plane in the Mesozoic strata of western China at various low temperatures using uniaxial and triaxial compression tests. Dai and Carlos Santamarina [8] conducted stress freezing tests on unsaturated fine sand under a nonlateral strain boundary condition to study the variation in the *P*-wave velocity in fine sand during loading, freezing, unloading, creep, and ice melting. They also investigated the influence of the loading and unloading rates on sand stiffness. Shogaki et al. [9] studied the dynamic strength and deformation properties of the sand layer in the Niigata East Port using a cyclic triaxial test. Hu et al. [10], Xu et al. [11], and Xu et al. [12] studied the

mechanical properties of saline frozen silty sandy sand using triaxial compression tests. Liu et al. [13] investigated the influence of the dynamic axial load on the dynamic properties and fatigue properties of frozen silty sand using cyclic triaxial tests. Ma et al. [14] used an environmental material test apparatus with three-point temperature control to perform triaxial compression tests for four temperatures and four confining pressures to examine the scattering of the mechanical properties of frozen sand. Liu et al. [15] conducted uniaxial compression tests for frozen sandstone samples and used X-ray computed tomography (X-ray CT) to study the effects of temperature and water content with uniaxial compression strength. Bai et al. [16] studied the microstructure and mechanical properties of frozen red sandstone samples by X-ray diffraction, mesostructure observation, and subzero rock triaxial test system. When a rock is broken by impact, the rock will break only when the stress is greater than the crushing strength of the rock. Thus, a rock test of a static or quasi-static load cannot be used to study the crushing strength or failure mode of the rock. Therefore, the study of the dynamic mechanical properties and failure modes of a rock mass under dynamic loading uses the comprehensive resistance index to measure the rock crushing difficulty during dynamic crushing. In this case, it is of great significance to study the dynamic mechanical properties and failure mode of frozen fine sandstone under an impact load in a low temperature environment.

At present, few studies have been conducted on the dynamic mechanical behavior of frozen fine sandstone. Yang et al. [17, 18] studied the dynamic compression characteristics of red sandstone, marble, and granite at different low temperatures using a split Hopkinson pressure bar (SHPB) testing device. Therefore, it is necessary to study the dynamic compression mechanical properties of frozen fine sandstone.

In this study, we used a Φ50 mm SHPB test device and a high-low temperature experimental chamber to make froze fine sandstone specimens at −15°C, −20°C, and −30°C. The impact compression tests were performed using an impact air pressure in 0.15 MPa, 0.25 MPa, and 0.3 MPa. The variations in dynamic peak stress, dynamic peak strain, failure morphology, and dynamic increase factor of frozen fine sandstone with temperature and strain rate are discussed and analyzed.

This paper is organized as follows. In Section 2, the preparation of the frozen fine sandstone specimens, the experimental procedure, and the test scheme are discussed. In Section 3, we present and discuss the experimental results, and we describe the dynamic mechanical properties and failure modes of the frozen fine sandstone specimens under lower temperatures and high strain rates. In Section 4, we present the conclusions reached based on the previously discussed results.

2. Impact Compression Tests of Frozen Fine Sandstone

2.1. Specimen Preparation. The rock samples were collected from the Paleogene strata of a coal mine in Ningxia, China. The geological data shows that the mine shaft passes through multiple layers of fine sandstone. The rock has poor cementation and softens easily in water. The maximum thickness is 40 m, and the water inrush rate is 3 to 6 m^3/s. Quicksand can form into construction disturbance, and the risk of water and sand inrush is extremely high. After a relevant technical demonstration, it was decided to adopt a construction method combining the freezing method and blasting excavation. The rock samples easily disintegrate into fine sand. The detailed physical indicators of fine sand are shown in Table 1.

The test specimens were prepared by remodeling the disintegrated fine sand. A Φ50 mm × 100 mm cylinder was used to prepare the quasi-static uniaxial compression specimens, and a Φ50 mm × 30 mm cylinder was used to prepare the impact specimens. The specimen preparation process was conducted as follows:

(1) The disintegrated fine sand was placed in an oven and heated for 12 h at a constant temperature of 105°C.

(2) An appropriate amount of distilled water was added to prepare a sand sample of a moisture content of 9.88%. Then, it was stirred evenly and sealed for 24 h to make the moisture content and structure of the sand uniform.

(3) The sand sample was stirred a second time, divided evenly into three parts, placed into the mold in layers, and compacted. Vaseline was applied to the surface to reduce the moisture loss of the specimen. To ensure the same degree of compaction, we poured each sand sample with a consistent quality into a custom abrasive tool to ensure the same depth each time, and then, we press the sand samples the same number of times. After sample compaction, we ensure that the same quality is achieved each time.

(4) The prepared sand sample in the mold was placed into the high-low temperature test chamber and frozen for 12 h at the required temperature (−15°C, −20°C, and −30°C). The mold was quickly removed, and then, the specimen was placed in a numbered sealed bag for moisture isolation, put back in the high-low temperature test chamber, and frozen at a constant temperature for more than 12 h.

A prepared frozen fine sandstone specimen is shown in Figure 1.

2.2. Static Compressive Strength Test. The static uniaxial compression test on the frozen fine sandstone was carried out using the W3Z-200 frozen soil triaxial test machine. During the test, the temperature of the test machine was set at −15°C, −20°C, and −30°C. Three specimens frozen at each temperature were selected, and axial loading of the specimens was performed by direct loading, with a loading strain rate of 1%/min. The test results are shown in Table 2.

Table 2 shows that the static compressive strength of the frozen fine sandstone gradually increased with decreasing temperature. A number of theoretical analyses and similar

Table 1: Sand parameters.

Dry density (g/cm^3)	Moisture content (%)	Void ratio (%)	Particle density (g/cm^3)	Liquid limit (%)	Plastic limit (%)
2.26	9.88	19.0	2.84	31.23	18.27

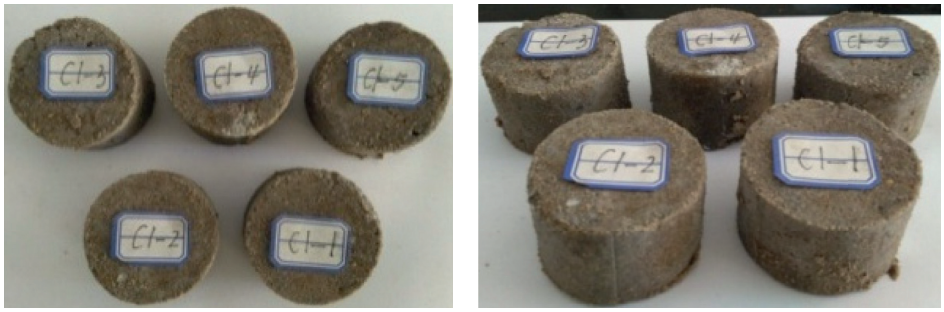

(a) (b)

Figure 1: Frozen fine sandstone specimens before the SHPB test. (a) Top view of the specimen. (b) Side view of the specimen.

Table 2: Uniaxial compression test results of the frozen fine sandstone.

Freezing temperature T (°C)	Static compressive strength σ_s (MPa)	Static average compressive strength $\overline{\sigma_s}$ (MPa)
−15	10.18 8.54 10.52	9.75
−20	12.43 14.93 12.98	13.45
−30	20.15 19.45 20.58	20.06

tests have shown that a decrease in temperature leads to a decrease in the unfrozen moisture content between the fine sand particles [19]. Part of the unfrozen moisture content is directly condensed from water vapor into ice, which generally exists in the form of ice monomers between the pores or shrinkage cracks of the sand particles, while the other part of the unfrozen moisture content is frozen in situ by liquid water into cementing ice, which exists at the contact or cementation interface between the sand particles, thereby enhancing the cementation effect of the ice in the frozen fine sandstone, giving it a high compressive strength and strong plastic deformation resistance.

2.3. SHPB Test System and Principle. The SHPB impact test technique is widely used to test the mechanical properties of materials at high strain rates [17–22]. The test was conducted using the Φ50 mm SHPB test system in the Impact Laboratory of Anhui University of Science and Technology. The test system consists of a dynamic loading module, a rate timing module, and a data acquisition and processing module, as shown in Figure 2. The bullet, incident bar, and transmission bar are all made of the same high-strength alloy steel, which has a density of 7800 kg/m^3, an elastic modulus of 210 GPa, Poisson's ratio of 0.30, and a wave velocity of 5190 km/s.

During the test, a specimen is placed between the incident bar and the transmission bar, and the bars are kept coaxial to ensuring that no scattering occurred during the propagation of the stress wave. The bullet is set to hit the incident bar in the axial direction at a certain initial velocity v, generating an incident pulse ε_i in the incident bar. When the stress wave reaches the specimen, it simultaneously generates a reflected pulse ε_r, which returns to the incident bar, and a transmitted pulse ε_t, which enters the transmission bar. The strain signals of the incident bar and the transmission bar is measured by strain gauge placed on these bars. Based on one-dimensional stress wave theory, the stress, strain, and strain rate of the specimen can be calculated using the following equations [23]:

$$\sigma_d(t) = \frac{S_B E}{2S_s}\left[\varepsilon_t(t) + \varepsilon_r(t) + \varepsilon_i(t)\right], \quad (1)$$

$$\dot{\varepsilon}_s(t) = \frac{C_0}{L_s}\left[\varepsilon_t(t) + \varepsilon_r(t) - \varepsilon_i(t)\right], \quad (2)$$

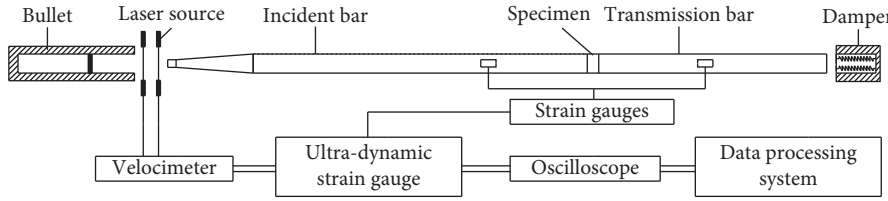

Figure 2: Schematic diagram of the SHPB test device.

$$\varepsilon_t(t) = \frac{C_0}{L_s}\int_0^t \left[\varepsilon_t(t) + \varepsilon_r(t) - \varepsilon_i(t)\right]\mathrm{d}t. \tag{3}$$

Here, S_B, E, and C_0 are the cross-sectional area, elastic modulus, and elastic compression wave velocity of the bar, respectively; $\varepsilon_i(t)$, $\varepsilon_r(t)$, and $\varepsilon_t(t)$ are the incident, reflected, and transmitted strain signals in the bar, respectively; and L_s and S_s are the length and cross-sectional area of the specimen, respectively.

2.4. Test Control Parameters and Test Scheme. Impact loads of 0.15 MPa, 0.25 MPa, and 0.3 MPa were applied to specimens with freezing temperatures of −15°C, −20°C, and −30°C to obtain the stress pulse data under the corresponding conditions. The tests were performed 3 times for each set of conditions, amounting to a total of 27 tests. In order to ensure that the impact velocity of the incident bar is the same for all three tests, the incident bar was kept at the same position within the emitter during all tests.

The SHPB dynamic test results must meet the following three basic requirements [23]: (a) the stress wave in the SHPB bar system conforms to the one-dimensional stress wave propagation characteristics; (b) the specimen is under stress equilibrium during the deformation process; and (c) the friction at each end of the specimen is negligible. To improve the accuracy of the SHPB dynamic test results in the frozen fine sandstone, the following measures were adopted in the test:

(1) To reduce the friction effect at the interface between the rock sample and the bar, a thin layer of Vaseline lubricant was evenly applied on the interface between the specimen and the two compression bars to reduce the friction between the specimen and the end face of the bar, the influence of the loading end restraint forces on the stress state distribution of the specimen, and the disturbance to the collected waveform.

(2) To reduce the influence of the dispersion effect during the test, according to the dispersion correction concept proposed by Frantz, a thin copper disc was attached to the impact end of the incident bar as a pulse shaper to increase the rise time of the pulse and thereby reduce the magnitude of the waveform oscillation [23].

(3) To eliminate the notable Pochhammer–Chree (PC) oscillation at the wave head, which causes the specimen to be in the repeated loading and unloading stage, an incident bar with a conical structure was used. Using an incident bar of a conical structure, the leading edge of incident waves which rose slowly was realized. As the loading section gradually rises, the waveform is flat and smooth, and the entire waveform has no obvious oscillations. It can meet the necessary time for the specimen to reach the requirement of stress uniformity, making it suitable for testing the dynamic stress-strain curve of the rock materials [23, 24].

3. Results and Analysis

3.1. Test Results. According to the basic principle of the SHPB test, the data were processed using the three-wave method to obtain the mechanical parameters, such as the dynamic stress and strain, of the frozen fine sandstone specimens. σ_d is the dynamic peak stress and ε_f is the corresponding strain of the specimen (that is, dynamic peak strain). The dynamic increase factor (DIF) is defined as the ratio of the dynamic compressive strength to the static compressive strength of the specimen, which represents the increase in the compressive strength of the specimen under the impact, that is,

$$\mathrm{DIF} = \frac{\sigma_d}{\sigma_s}, \tag{4}$$

where σ_d is the dynamic compressive strength of the specimen and σ_s is the static compressive strength of the specimen.

The typical waveform of the frozen fine sandstone specimen obtained from the test is shown in Figure 3. As can be seen from Figure 3, both the incident and reflected waves are rectangular pulses. The higher the impact velocity is, the larger the amplitude of the incident wave is. The transmitted wave has a waveform that is unloaded halfway and has a small amplitude, which is reduced compared to that of the incident wave. In addition, it can be seen from the figure that the reflected wave has a good plateau at the top. So, it can be concluded that constant strain rate loading was achieved in the SHPB impact test [23].

The typical dynamic stress equilibrium waveform of the frozen fine sandstone specimen obtained from the test is shown in Figure 4. The figure contains incident wave (Inc), reflected wave (Re), and comparison wave (Inc + Re). It can be seen from Figure 4 that the time-history curve of transmission waves to coincide with comparison wave basically. It can be considered that the specimen is in a state of stress balance during deformation.

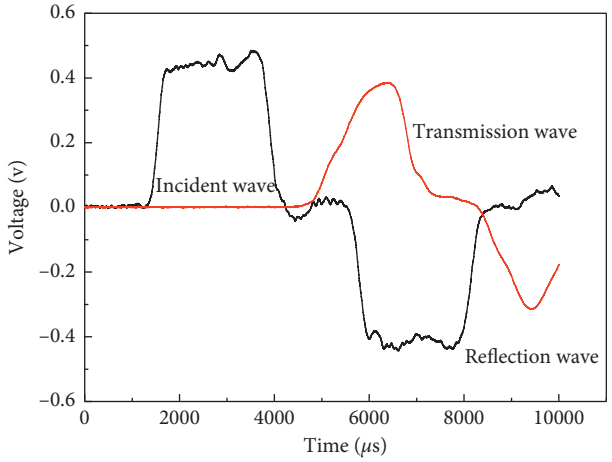

Figure 3: Typical waveform.

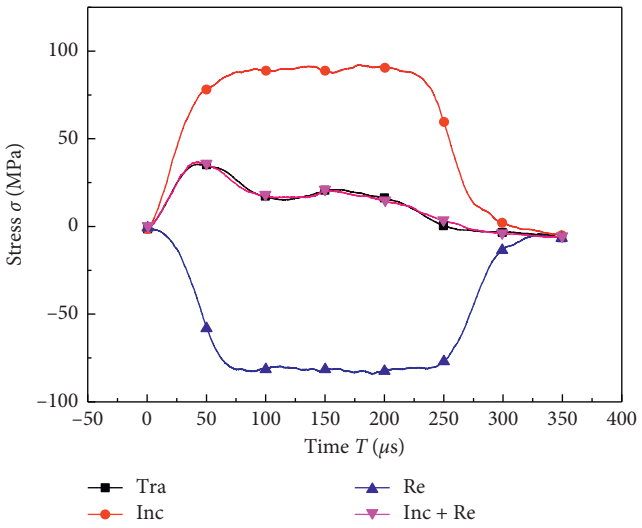

Figure 4: Typical dynamic stress equilibrium waveform.

The measured data were analyzed using equations (1)–(3) to obtain the average strain rate $\dot{\varepsilon}$, the dynamic peak stress σ_d, and the dynamic peak strain ε_f of the specimen at different freezing temperatures T and impact velocities v. The typical test results are shown in Table 3.

3.2. Dynamic Stress-Strain Curve. A typical dynamic stress-strain curve obtained from the test is shown in Figure 5.

As can be seen from Figure 5, the entire testing process of the frozen fine sandstone specimens at different temperatures (−15°C, −20°C, and −30°C) under different strain rates $\dot{\varepsilon}$ can be divided into four stages (as shown in Figure 5(d)). Stage I (OA) is the compaction stage. The stress-strain curve has a small slope and is to bent upward, that is, its line slope gradually increases. This stage reflects the inelastic deformation caused by the closing of the initial defects (microcracks and microvoids) in the frozen fine sandstone specimen during compression. Because the strain rate of the dynamic load is much higher than that under the static or quasi-dynamic load, the microcracks in the frozen fine

Table 3: Typical SHPB tests results.

Number	T (°C)	v (m·s^{-1})	$\dot{\varepsilon}$ (s^{-1})	σ_d (MPa)	ε_f	DIF
A1-1	−15	1.98	28	26.38	0.007	2.71
A1-2		2.12	32	26.77	0.009	2.75
A1-3		2.28	34	30.92	0.013	3.17
A2-1		2.74	41	33.78	0.010	3.46
A2-2		2.87	42	37.63	0.012	3.86
A2-3		3.28	47	38.35	0.016	3.93
A3-2		3.83	64	57.72	0.015	5.92
A3-3		4.52	70	55.34	0.016	5.68
B1-1	−20	2.15	33	37.34	0.009	2.78
B1-2		2.28	34	42.26	0.012	3.14
B1-3		2.31	36	42.19	0.008	3.14
B2-1		3.28	48	51.44	0.020	3.82
B3-1		3.99	60	58.33	0.017	4.34
B3-2		4.21	64	62.58	0.016	4.65
B3-3		4.48	67	60.37	0.017	4.49
C1-1	−30	1.40	31	55.49	0.006	2.77
C1-3		2.17	36	55.48	0.009	2.77
C2-1		3.01	46	71.55	0.010	3.57
C2-2		3.03	46	71.63	0.016	3.57
C2-3		3.34	54	72.99	0.014	3.64
C3-1		3.94	58	78.06	0.014	3.89
C3-2		4.96	74	80.15	0.017	4.00
C4-1		5.51	83	87.79	0.025	4.38

sandstone are closed to a relatively small extent, so this stage is not obvious, but it is still present on the stress-strain curve. Stage II (AB) is the elastic deformation stage. The stress state of the impact load on the specimen is lower than the yield state of the material, forming an elastic stress wave. The stress-strain relationship enters the linear elastic deformation stage, at which the compression modulus of the specimen reflects the true elastic modulus. Stage III (BC) is the plastic deformation stage. The stress-strain relationship is no more linear, and the curve is bent downward with a gradually decreasing slope. Due to the propagation of the stress waves, the cementation of the ice crystals in the specimen is gradually destroyed. As a result, the material yield strength decreases, which is the plastic stage before yielding is reached, and the specimen undergoes irreversible plastic deformation. In this stage, the microcracks at the specimen gradually nucleate and propagate, and the plastic deformation stage ends at the peak stress. Stage IV (CD) is the failure stage. In this stage, the specimen is damaged, its stress decreases in increasing deformation, and the curve has a negative slope.

As can be seen from Figures 5(a)–5(c), under different test conditions, the variation patterns of the stress-strain curves of the specimens are similar, and the strain on the elastic deformation stage is smaller than that in the plastic deformation stage. As can be seen from Figure 5(c), the stress-strain curve of the frozen fine sandstone specimen at a freezing temperature of −30°C is similar in shape to the stress-strain curve of ice subjected to impact compression tests at low temperatures [25, 26]. Because the frozen fine sandstone specimen is a multiphase complex consisting of

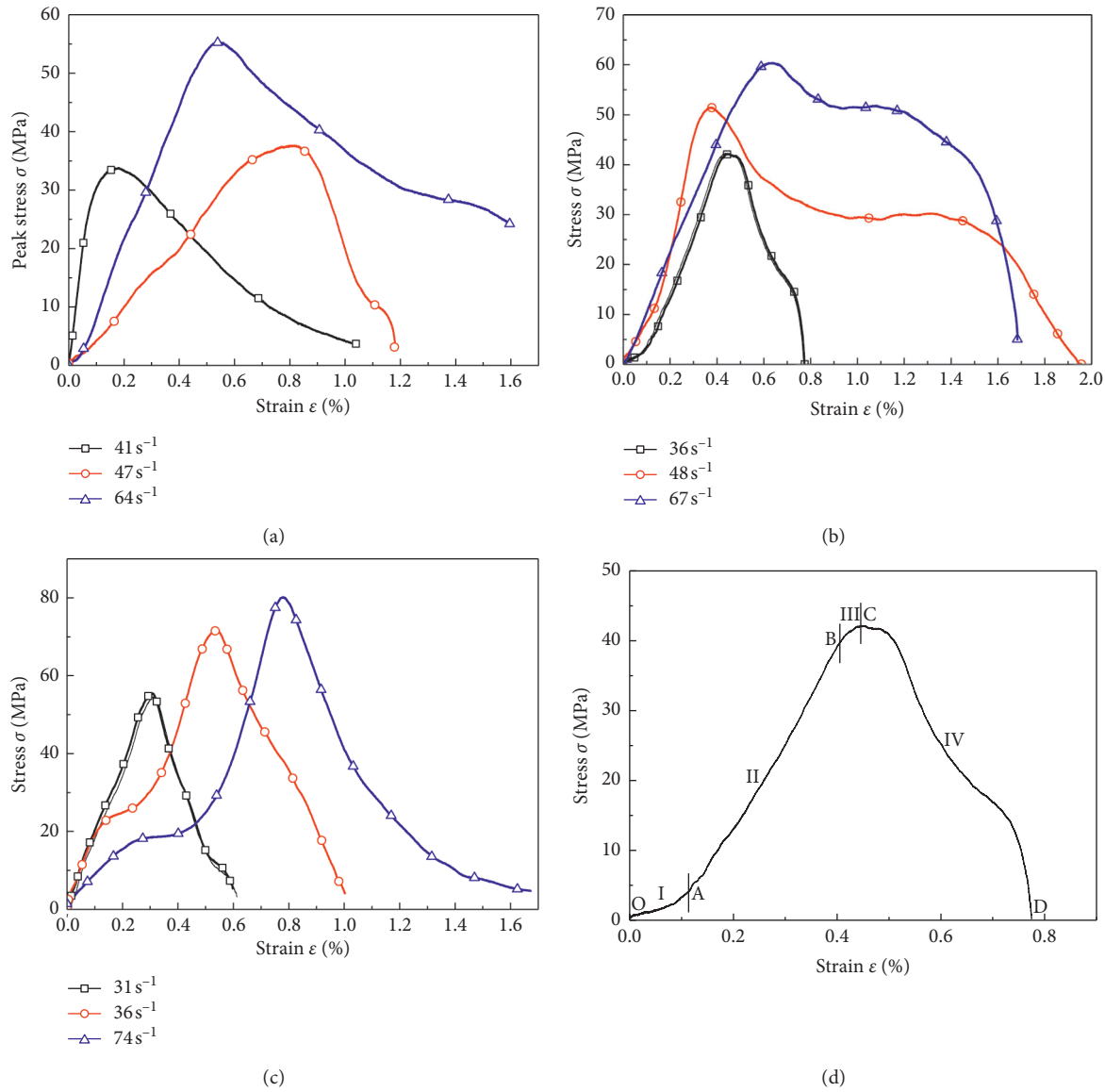

Figure 5: Typical strain-stress curves. (a) −15°C. (b) −20°C. (c) −30°C. (d) The different stages.

fine sand particles of ice cemented between them [27], it can be inferred that the strength properties of the frozen fine sandstone at −30°C mainly depend on the properties of the cementing ice between the sand particles, which is consistent with previous results [28].

3.3. Dynamic Peak Stress. The variation in the dynamic peak stress of the specimens at different temperatures with the strain rate is shown in Figure 6.

As can be seen from Figure 6, the dynamic peak stress of the fine sandstone specimens increases linearly with the increasing strain rate. The fitted straight lines $\sigma_d - \dot{\varepsilon}$ associated with −20°C and −30°C are both located above the fitted straight line associated with −15°C, that is, the σ_d in this temperature range is higher than the σ_d at −15°C for the same $\dot{\varepsilon}$. Among them, the fitted straight line $\sigma_d - \dot{\varepsilon}$ associated with −30°C is at the top of the fitted straight lines associated with the three temperatures, that is, it has the largest value of the curve $\sigma_d - \dot{\varepsilon}$; with $\dot{\varepsilon} = 31$ to $83\,s^{-1}$, $\sigma_d = 55.49$ to 87.79 MPa, and σ_d is increased by 44.8% to 107.3% compared with that of the frozen fine sandstone at −15°C for the same $\dot{\varepsilon}$. This shows that, in the temperature range of $-30°C \le T \le -15°C$, a decrease in temperature has a strengthening effect on the dynamic compressive strength of the frozen fine sandstone specimens, and this temperature effect is the most remarkable at −30°C. Regression analysis of the test gives

$$\sigma_d = a\dot{\varepsilon} + b, \tag{5}$$

where σ_d is the dynamic peak stress; $\dot{\varepsilon}$ is the strain rate; and a and b are the coefficients related to the fitted straight line. The values of the frozen fine sandstone specimens at different low temperatures are reported on Table 4.

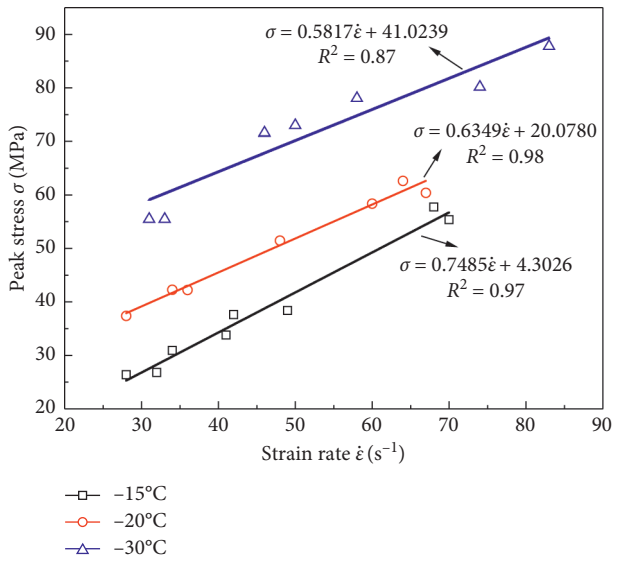

Figure 6: Relationship between the peak stress and the strain rate.

As can be seen from Table 4, the minimum value of the fitting correlation coefficient R^2 of the dynamic peak stress σ_d and the strain rate $\dot{\varepsilon}$ of the frozen fine sandstone specimens at different low temperatures is 0.87, indicating that there is a significant correlation between the two. The fitted straight line $\sigma_d - \dot{\varepsilon}$ is shown in Figure 6.

As can be seen from Table 4, temperature has little influence on parameter a, so the average value (0.6580) of a at the three temperatures can be used. Parameter a reflects the influence of the strain rate for the dynamic compressive strength of the frozen fine sandstone. The temperature has a high influence on parameter b, and the value of b increases linearly from decreasing temperature:

$$B = -2.3976T - 30.1462,$$
$$R^2 = 0.98\,(-30^{\circ}\mathrm{C} \le T \le -15^{\circ}\mathrm{C}), \quad (6)$$

where b is the influence parameter of temperature on the dynamic compressive strength of the frozen fine sandstone and T is the freezing temperature.

By substituting equation (6) into equation (5), the relational expression of the dynamic peak stress of the specimen to the freezing temperature and strain rate for the test conditions ($-30^{\circ}\mathrm{C} \le T \le -15^{\circ}\mathrm{C}$, $28\,\mathrm{s}^{-1} \le \dot{\varepsilon} \le 83\,\mathrm{s}^{-1}$) can be obtained as

$$\sigma_d = 0.658\dot{\varepsilon} - 2.3796T - 30.1462, \quad (7)$$

where σ_d is the dynamic peak stress of the specimen.

To quantify the influence of temperature on the dynamic compressive strength of the frozen fine sandstone specimens, the dynamic peak stress of the specimens with a certain range of strain rates (with a fluctuation of $5\,\mathrm{s}^{-1}$) is evaluated, as shown in Table 5, and then, the variation in the average dynamic peak stress of the frozen fine sandstone specimens with different strain rate ranges as a function of temperature ($\overline{\sigma_d}$—T curve) is obtained, as shown in Figure 7.

Table 4: Fitting parameters for the peak stress and the strain rate.

Temperature T (°C)	a (MPa·s)	b (MPa)	Correlation coefficient R^2
−15	0.582	41.024	0.97
−20	0.635	20.078	0.98
−30	0.749	4.303	0.87

Table 5: Average peak stress of the frozen fine sandstone.

$\dot{\varepsilon}$ (s^{-1})	T (°C)	σ_d (MPa)	$\overline{\sigma_d}$ (MPa)
28		26.38	
32	−15	26.77	28.02
34		30.92	
33	−20	37.34	39.80
34		42.26	
31	−30	55.49	55.49
33		55.48	
49	−15	38.35	38.35
48	−20	51.44	51.44
50	−30	72.99	72.99
68	−15	57.72	56.53
70		55.34	
64	−20	62.58	61.48
67		60.37	
74	−30	80.15	80.15

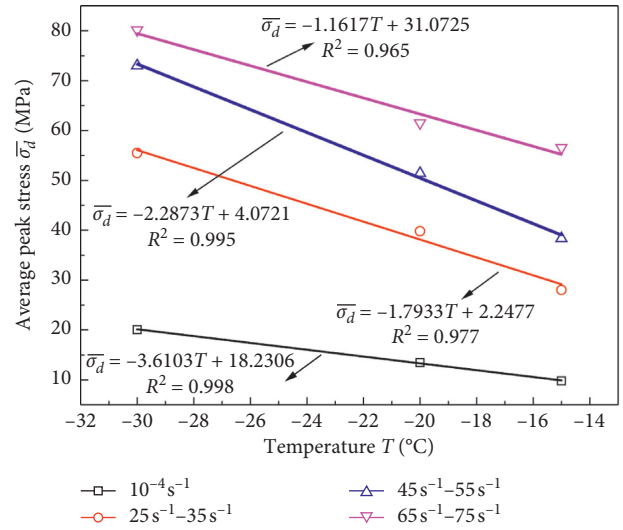

Figure 7: Relationship between the average dynamic peak stress and the temperature.

As can be seen from Figure 7, at the approximate strain rate, the peak stress is very sensitive to the freezing temperature, i.e., it increases sharply as the freezing temperature decreases. Under different strain rates, the higher the strain rate is, the more dramatic the variation in dynamic peak stress with the initial freezing temperature is, that is, as the initial loading rate increase, the sensitivity of the frozen fine sandstone to temperature becomes increases. As can be seen from Figure 7, the dynamic compressive strength of the specimen within the tested strain rate range of −30°C is higher than the dynamic compressive strength of the

specimen with the highest test strain rate for −15°C. Therefore, for the two test temperatures, temperature is the main factor affecting the dynamic compressive strength of the specimens. However, frozen fine sandstone is a complex structure composed of frozen ice and fine sandstone [29], and the content of unfrozen water decreases from decreasing temperature [30]. The unfrozen water in the frozen fine sandstone determines the migration of the liquid water in the frozen fine sandstone. In addition, as the temperature decreases, the liquid water changes from the liquid phase to the solid phase, that is, part of the unfrozen water within the pores of the fine sandstone particles is converted into pore ice, which leads to an increase in the dynamic compression strength of the specimen.

3.4. Dynamic Fragmentation Degrees. The typical fragmentation degrees of specimens under different test conditions are shown in Table 6. As can be seen from Table 6, at the same temperature, as the strain rate increased, the number of fracture cracks in the specimen gradually increased, and the size of the fragments decreased. At −15°C, under a strain rate of 32 s^{-1}, there were no notable macrocracks on the surface of the specimen. Under a strain rate of 34 s^{-1}, the failure plane of the specimen was approximately parallel to the axial direction and the specimen was broken into two pieces. Under a strain rate of 47 s^{-1}, the specimen was broken into 7 pieces. Under a strain rate of 70 s^{-1}, the specimen was crushed. At −20°C and −30°C, as the strain rate increased, the fracture morphology of the specimen after failure showed the same development trend. The typical failure modes of specimens are mainly axial splitting tensile failure and compression crushing failure. The failure mode of the specimen depends on the strain rate level. When the strain rate is within a certain low range, the frozen fine sandstone specimen mainly fails in the axial splitting tensile failure. In general, the failure plane is approximately parallel to the axial direction and the specimen is broken into two or more pieces, which is characteristic of a typical tensile splitting failure. This is because the resistance of the frozen fine sandstone to tension is far less than its resistance to compression. As the strain rate increased, the axial compression loads increased rapidly under a large impact load, and the frozen fine sandstone exhibited a compression crushing failure. (1) At −15°C, the specimens under impact compressions of 34 s^{-1} to 64 s^{-1} failed in the axial splitting tensile failure. In Table 6, the specimens under 34 s^{-1} and 47 s^{-1} failed in this mode. When the strain rate reached 70 s^{-1}, the specimens failed in the compression crushing failure. In Table 6, the specimen under 70 s^{-1} failed in this mode. (2) At −20°C, the specimens under impact compressions of 36 s^{-1} to 64 s^{-1} failed in the axial splitting tensile failure. In Table 6, the specimens under 36 s^{-1} and 48 s^{-1} failed in this mode. When the strain rate reached 67 s^{-1}, the specimens failed in the compression crushing failure. In Table 6, the specimen under 67 s^{-1} failed in this mode. (3) At −30°C, the specimens under impact compressions of 46 s^{-1} to 58 s^{-1} failed in the axial splitting tensile failure. In Table 6, the specimens under 46 s^{-1} to 54 s^{-1} failed in this mode. When the strain rate reached 74 s^{-1}, the specimens failed in the compression crushing failure. In Table 6, the specimen under 74 s^{-1} failed in this mode.

The underlying mechanism is analyzed as follows. At low temperatures, the macroscopic fragmentation degrees of the specimen under impact compression are the result of the initiation, evolution, propagation, and coalescence of the internal microcracks of the frozen fine sandstone under the combined action of temperature and impact load. At different stages of impact loading, crack propagation reaches different levels, leading to different failure forms of the frozen fine sandstone. At a low strain rate level, the resulting cracks are all from the tip of an existing defect, and it extends along the direction parallel to the compressive stress and it has obvious direction. The main cracks do not participate in the failure of the material, while the development and aggregation of microcracks with less energy absorption plays a major role in the failure of the frozen fine sandstone, resulting in a small degree of failure of the frozen fine sandstone and exhibiting the axial splitting tensile failure. At a high strain rate level, after the axial splitting and tensile failure of the specimen, the stress wave propagated into the rock continued to increase, more and more microcracks absorb energy, propagate to coalesce into a main crack, and they participate in the failure of the material, resulting in more severer crushing of the material and exhibiting the compression crushing. However, a decrease in temperature can increase the strength of the cementing ice between the sand particles of the material, enhancing the mechanical properties of the specimen, and thus, decreasing the severity of the impact failure.

3.5. Dynamic Increase Factor. The strength of the specimen increases with decreasing temperature under both dynamic and static loads. The variation in the dynamic increase factor (DIF) of the specimens at different temperatures with strain rate $\dot{\varepsilon}$ was obtained using equation (4), as shown in Figure 8.

Specifically, the relationship between the DIF and the loading strain rate for the three temperatures is

$$\begin{aligned} &-15^{\circ}\mathrm{C}: \mathrm{DIF} = 0.0768\dot{\varepsilon} + 0.4412\left(28\ \mathrm{s}^{-1} \le \dot{\varepsilon} \le 83\ \mathrm{s}^{-1}\right), \\ &-20^{\circ}\mathrm{C}: \mathrm{DIF} = 0.0499\dot{\varepsilon} + 1.3277\left(28\ \mathrm{s}^{-1} \le \dot{\varepsilon} \le 83\ \mathrm{s}^{-1}\right), \\ &-30^{\circ}\mathrm{C}: \mathrm{DIF} = 0.029\dot{\varepsilon} + 2.0453\left(28\ \mathrm{s}^{-1} \le \dot{\varepsilon} \le 83\ \mathrm{s}^{-1}\right). \end{aligned} \quad (8)$$

As can be seen from Figure 8, under a dynamic load impact, the DIF increases linearly with increasing strain rate $\dot{\varepsilon}$, and the growth rate of the DIF decreases as the temperature decreases. When the strain rate is around 33 s^{-1}, the DIF of the three lower temperatures frozen fine sandstone samples are almost the same, approximately 3.0. However, as shown in Figure 8, with the lower the temperature, the growth rate of DIF is smaller. Analyze the cause. With the decrease of temperature, the content of pore water in the specimen turned into frozen ice increased, and the initial dynamic compressive strength of the specimen was relatively high. Therefore, it was more difficult to rapidly improve the DIF value of dynamic strength of the specimen. Meanwhile, with the decrease of temperature, the brittleness of the specimen became larger, and under the effect of high strain rate, the tensile stress was less.

Table 6: Fragmentation degrees under different conditions.

Temperature (°C)	Fragmentation degrees of the specimen			
−15	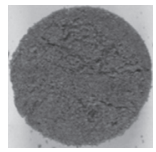 $\dot{\varepsilon}$: 32 s^{-1}	 $\dot{\varepsilon}$: 34 s^{-1}	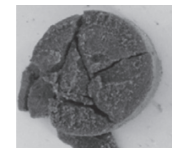 $\dot{\varepsilon}$: 47 s^{-1}	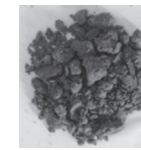 $\dot{\varepsilon}$: 70 s^{-1}
−20	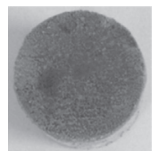 $\dot{\varepsilon}$: 33 s^{-1}	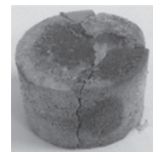 $\dot{\varepsilon}$: 36 s^{-1}	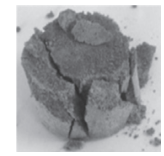 $\dot{\varepsilon}$: 48 s^{-1}	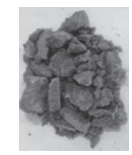 $\dot{\varepsilon}$: 67 s^{-1}
−30	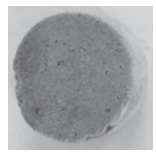 $\dot{\varepsilon}$: 31 s^{-1}	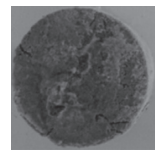 $\dot{\varepsilon}$: 46 s^{-1}	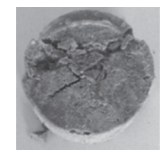 $\dot{\varepsilon}$: 54 s^{-1}	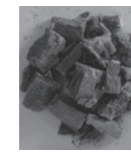 $\dot{\varepsilon}$: 74 s^{-1}

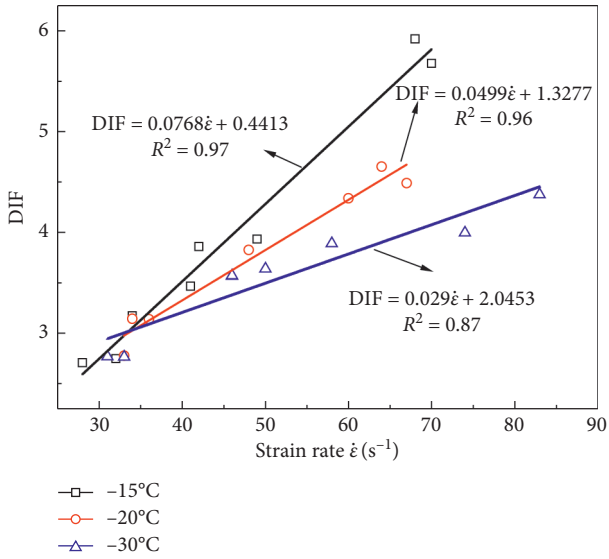

Figure 8: Relationships between the DIF and the strain rate at different temperatures.

In this paper, we studied the dynamic mechanical properties and failure modes of frozen fine sandstone specimens under lower temperatures and high strain rates. The experimental results reveal some changes in the related regularity. However, during the construction of a coal mine shaft, the influence of the ground stress on the frozen wall is not negligible. Future research should focus on the dynamic mechanical properties and failure modes of frozen fine sandstone under confining pressure and axial compression. Furthermore, the study of dynamic crack propagation with a high-speed video system would improve our understanding of the failure mechanism and failure mode of dynamic fine sandstone under impact loading.

4. Conclusions

An SHPB test system was used to perform impact compression tests of frozen fine sandstone specimens within a strain rate range of 28 s^{-1} to 83 s^{-1} at −15°C, −20°C, and −30°C. The following conclusions are drawn:

(1) Under low temperature conditions, the dynamic peak stress of the frozen fine sandstone specimens increase linearly from increasing strain rate. Under the same strain rate, the dynamic peak stress gradually increases from decreasing temperature.

(2) The fragmentation degrees of the specimen are mainly divided into the axial splitting tensile failure and the compression crushing failure. Under the same temperature condition, with the increase of strain rate, the crack of the specimen increases gradually and the crushing size decreases.

(3) The DIF of frozen fine sandstone has a linear relationship with the strain rate for low temperatures.

Data Availability

All the data used to support the findings of this study are included within the article.

Conflicts of Interest

The authors declare that there are no conflicts of interest in the publication of this paper.

References

[1] W. H. Sui, G. T. Cai, and Q. H. Dong, "Experimental research on critical percolation gradient of quicksand across overburden fissures due to coal mining near unconsolidated soil

layers," *Chinese Journal of Rock Mechanics and Engineering*, vol. 26, no. 10, pp. 2084–2091, 2007.

[2] X. Yang, Z. H. Xu, T. H. Yang, B. Yang, and W. H. Shi, "Incipience condition and migration characteristics of aeolian-sand aquifer in a typical western mine," *Rock and Soil Mechanics*, vol. 39, no. 1, pp. 21–28, 2018.

[3] Q. Zong, J. G. Fu, and H. S. Xu, "Study and application of frozen soil blasting technique in shaft," *Rock and Soil Mechanics*, vol. 28, no. 9, pp. 1992–1996, 2007.

[4] J. X. Ren, J. L. Sun, K. Zhang et al., "Mechanical properties and temperature field of inclined frozen wall in water-rich sand stratum," *Rock and Soil Mechanics*, vol. 38, no. 5, pp. 1405–1412, 2017.

[5] D. W. Li, R. H. Wang, and J. H. Fan, "Nonlinear rheological model for frozen soft rock during Cretaceous period," *Chinese Journal of Geotechnical Engineering*, vol. 33, no. 3, pp. 398–403, 2011.

[6] G. S. Yang and X. T. Lv, "Experimental study on the sandy mudstone mechanical properties of shaft sidewalls under the frozen conditions," *Journal of Mining & Safety Engineering*, vol. 29, no. 4, pp. 492–496, 2012.

[7] B. Liu, N. Liu, D. Y. Li, S. Wang, and Y. C. Liu, "Strength test on frozen cracked red sandstone combined with ice," *Journal of China Coal Society*, vol. 41, no. 4, pp. 843–849, 2016.

[8] S. Dai and J. Carlos Santamarina, "Stiffness evolution in frozen sands subjected to stress changes," *Journal of Geotechnical and Geoenvironmental Engineering*, vol. 143, no. 9, pp. 04017042–04017047, 2017.

[9] T. Shogaki, Y. Nakano, and T. Yoshizu, "Estimating in situ dynamic strength and deformation properties of Niigata East Port sand deposits," *Soils and Foundations*, vol. 57, no. 6, pp. 947–964, 2017.

[10] K. Hu, X. Chen, and J. Chen, "Laboratory investigation of deformation and strength characteristics of saline frozen silty sand," *Soil Mechanics and Foundation Engineering*, vol. 54, no. 2, pp. 102–109, 2017.

[11] J. Xu, H. Liu, and X. Zhao, "Study on the strength and deformation property of frozen silty sand with NaCl under triaxial compression condition," *Cold Regions Science and Technology*, vol. 137, pp. 7–16, 2017.

[12] X. Xu, Y. Wang, R. Bai, H. Zhang, and K. Hu, "Effects of sodium sulfate content on mechanical behavior of frozen silty sand considering concentration of saline solution," *Results in Physics*, vol. 6, pp. 1000–1007, 2016.

[13] E. Liu, Y. Lai, M. Liao, X. Liu, and F. Hou, "Fatigue and damage properties of frozen silty sand samples subjected to cyclic triaxial loading," *Canadian Geotechnical Journal*, vol. 53, no. 12, pp. 1939–1951, 2016.

[14] L. Ma, J. Qi, F. Yu, and X. Yao, "Experimental study on variability in mechanical properties of a frozen sand as determined in triaxial compression tests," *Acta Geotechnica*, vol. 11, no. 1, pp. 61–70, 2016.

[15] B. Liu, Y. D. Sun, B. Wang, Y. Han, R. Zhang, and J. Wang, "Effect of water content on mechanical and electrical characteristics of the water-rich sandstone during freezing," *Environmental Earth Sciences*, vol. 79, no. 10, pp. 1–14, 2020.

[16] Y. Bai, R. L. Shan, Y. Ju, Y. Wu, P. Sun, and Z. Wang, "Study on the mechanical properties and damage constitutive model of frozen weakly cemented red sandstone," *Cold Regions Science and Technology*, vol. 171, Article ID 102980, 2020.

[17] Y. Yang, *Experimental study on dynamic mechanical properties of rock under low temperature*, Ph.D. thesis, China University of Mining and Technology, Beijing, China, 2016.

[18] Y. Yang, R. S. Yang, J. G. Wang, S. Z. Fang, and N. N. Zhang, "Experimental study on dynamic mechanical properties of red sandstone under low temperatures," *Journal of China Coal Society*, vol. 43, no. 4, pp. 967–975, 2018.

[19] X. Xu, Y. Wang, Z. Yin, and H. Zhang, "Effect of temperature and strain rate on mechanical characteristics and constitutive model of frozen Helin loess," *Cold Regions Science and Technology*, vol. 136, pp. 44–51, 2017.

[20] F.-Q. Gong, X.-F. Si, X.-B. Li, and S.-Y. Wang, "Dynamic triaxial compression tests on sandstone at high strain rates and low confining pressures with split Hopkinson pressure bar," *International Journal of Rock Mechanics and Mining Sciences*, vol. 113, pp. 211–219, 2019.

[21] R. Chen, W. Yao, F. Lu, and K. Xia, "Evaluation of the stress equilibrium condition in axially constrained triaxial SHPB tests," *Experimental Mechanics*, vol. 58, no. 3, pp. 527–531, 2018.

[22] S. Luo and F. Gong, "Experimental and numerical analyses of the rational loading waveform in SHPB test for rock materials," *Advances in Civil Engineering*, vol. 2018, Article ID 3967643, 13 pages, 2018.

[23] X. B. Li, *Rock Dynamics: Fundamentals and Applications*, Science Press, Beijing, China, 2014.

[24] Q. Ping, Q. Y. Ma, and P. Yuan, "Energy dissipation analysis of stone specimens in SHPB tensile test," *Journal of Mining & Safety Engineering*, vol. 30, no. 3, pp. 401–407, 2013.

[25] Y. Wang, Y. L. Li, and C. X. Liu, "Dynamic mechanical behaviors of ice at high stain rates," *Explosion and Shock Waves*, vol. 31, no. 2, pp. 215–219, 2011.

[26] Y. Zhang, Y. Li, Z. Tan, and K. Jin, "Mechanical behavior and failure mechanism of ice at cryogenic temperatures under uniaxial compression," *Chinese Journal of Solid Mechanics*, vol. 39, no. 5, pp. 530–538, 2018.

[27] Y. Q. Tang and J. Z. Li, "Test method and application for microstructures of undisturbed silty sand and sandy silt," *Environmental Earth Sciences*, vol. 77, pp. 654–657, 2018.

[28] V. I. Aksenov, S. G. Gevorkyan, and V. V. Doroshin, "Dependence of strength and physical properties of frozen sands on moisture content," *Soil Mechanics and Foundation Engineering*, vol. 54, no. 6, pp. 420–424, 2018.

[29] W. Ma and D. Y. Wang, *Frozen Soil Mechanics*, Science Press, Beijing, China, 2014.

[30] X. Z. Xu, J. C. Wang, and L. X. Zhang, *Physics of Permafrost*, Science Press, Beijing, China, 2010.